Fe₃O₄ Nanorods and Polyhedrons as Anodes for Lithium Ion Batteries: Morphology and Electrochemical Properties

Zhengguan Xu[1,§], Laiying Jing[2,§], Xiang Zheng[1], Yuhao Dong[1], Yapeng Yuan[1], Zongyu Wang[1], Xuehua Liu[1], Aiping Fu[2,3], Hongliang Li[1,3,]*

[1] Institute of Materials for Energy and Environment, College of Materials Science and Engineering, Qingdao University, Qingdao 266071, China
[2] School of Materials Science and Engineering, Qilu University of Technology (Shandong Academy of Sciences), Jinan 250353, China
[3] College of Chemistry and Chemical Engineering, Qingdao University, Qingdao 266071, China
[4] State Key Laboratory of Biopolysaccharide Fiber Forming and Eco-Textile, Qingdao University, Qingdao 266071, China
[§] These authors contribute equally to this work
[*] E-mail: lhl@qdu.edu.cn

A solvothermal process with temperature up to 350°C has been exploited for the fabrication of Fe₃O₄ with diverse morphologies. The influences of solvothermal temperature and treating time on the composition, morphology and electrochemical properties of the resulted Fe₃O₄ samples have been studied. Electrochemical properties of the obtained Fe₃O₄ with morphologies of nanorods, nanoplates and polyhedrons have been explored as anode materials for lithium ion batteries. It has been found that two typical morphologies of nanorods and polyhedrons can be resulted by varying the solvothermal treating times from 12 to 72 h. The morphology evolution of the Fe₃O₄ sample upon treating times has been discussed by analyzing the control experiments. The Fe₃O₄ nanorods obtained under the favorite condition, i.e. solvothermally at 350°C for 12h and then calcined at 500°C for 2h delivered a superior reversible capacity of 807.9 mAh g⁻¹ at 0.2 A g⁻¹ even after 200 charging-discharging cycles, demonstrating excellent cycle stability. It shows also satisfied rate capability of 360 mAh g⁻¹ at current density of 2 A g⁻¹. The superior electrochemical performance of the Fe₃O₄ nanorods has been discussed from the structure character and the composition aspects.

1. INTRODUCTION

Lithium Ion batteries (LIBs) have now been the research focus in fields of energy storage due to the fast development of portable electronic devices and electric vehicles [1, 2]. Unfortunately, the current

materials cannot satisfy one's demand for high capacity. To overcome this problem, worldwide endeavors are devoted to explore advanced active materials for LIBs. Transition metal oxides are now being considered as s kind of promising anode materials owe to their high energy density, satisfied safety, eco-friendly and inexpensiveness [3-8]. Of all the candidates, magnetite (Fe_3O_4) is the most promising one owe to its high theoretical capacity of 926 mAh g^{-1}, which much higher than carbonaceous substances[9-13]. Nevertheless, its potential utilizations are because of the poor electrical conductivity and obvious volume effect. In order to solve the above-mentioned obstacles and obtain excellent electrochemical performance, various methods for the synthesis of Fe_3O_4 nanostructures have been pursued. For example, Hao Wu et al. prepared a three-dimensionally porous structure of Fe_3O_4, which shows high reversible capacity as electrode of LIBs [14,15]. Ke's group reported an architecture of nanosized Fe_3O_4 array which exhibited a stable capacity of about 750 mA g^{-1} when it was utilized as anode for LIBs[16]. Peihao Lian et al. fabricated a Fe_3O_4-graphene nanocomposite which also show excellent electrochemical properties[17].

Normally, Fe_3O_4 can be fabricated via hydrothermal or solvothermal with temperature below 200°C because of the low softening point of the applied autoclave liner polytetrafluoroethylene (240°C). Herein, Ferrous oxalate dihydrate is used as source of iron and the tetrahydrofuran has been applied as solvent for the preparation of the Fe_3O_4. Fe_3O_4 with morphology of nanorods and polyhedrons have been obtained via a high-temperature solvothermal method at 350°C and by simply tuning the treating time. In comparison with the previous studies, one character of this method is the temperature of solvothermal treatment and the morphology evolution under such a high temperature. Definitely, such a morphology change cannot be achieved below 300°C. The other merit of this method is that no additional carbon source is needed for the reaction, however, the conductivity of the resulted Fe_3O_4 still can be guaranteed which might be due to an in-situ mixing of carbon with Fe_3O_4. Usually, external carbon sources are demanded to improve the conductivity of pristine Fe_3O_4. The organic moieties in the applied organic iron salt precursor could decompose under such a high temperatures and form carbon in-situ and well-distributed among the Fe_3O_4. As results, the Fe_3O_4 with the wire type structure shows superior reversible capacity and high cycle stability.

2. EXPERIMENTAL SECTION

2.1. Materials

Ferrous oxalate dihydrate (Beijing Jingqiu Chemical Industry Co., Ltd), Cetyltrimethyl ammonium bromide and Tetrahydrofuran (Sinopharm Chemical Reagent Co., Ltd) are of AR grade and utilized no further purification.

2.2. Synthesis of Fe₃O₄ nanorods and Fe₃O₄ polyhedrons

The Fe_3O_4 nanorods were synthesize by a simple solvothermal treatment. 0.2g of ferrous oxalate dihydrate, 0.005g of hexadecyl trimethyl ammonium bromide (CTAB) were added to 5 ml of tetrahydrofuran with intense stirring. After a stirring of 20 min, the solution was poured into a stainless

autoclave with Swagelok structure (a homemade cell with a capacity of about 8 mL and can be used at elevated temperatures up to 450°C). Then the cell was placed into a thermostatic oven and treated at 350°C for 6, 12, 24, 36, and 72 h. The obtained grey sedimentations were separated by centrifugation and washed twice with water and ethanol, respectively. The samples obtained at this stages were named as Fe_3O_4-X (X = 6, 12, 24, 36 and 72, which stands for the thermal treating time). Then they were calcined in a quartz tube at 500°C under a nitrogen atmosphere for 2h, and the corresponding products were obtained and labelled as Fe_3O_4-X-500. As control sample, Fe_3O_4 was synthesized by the same strategy but was treated solvothermally at a temperature of 300 °C for 12 h and the obtained sample was labelled as Fe_3O_4-12(300).

2.3. Characterization

The phase and composition information of the samples are measured by a Rigaku ultima IV X-ray diffractometer (XRD, Cu-Kα radiation λ=0.15418). The porosity is investigated by a TriStar 3000 Surface Area and Pore Analyzer and the data are calculated by the Brunauer-Emmett-Teller (BET) model. The morphologies of the samples are observed with a JSM-7800F scanning electron microscopy (SEM) and a JEM-2100F transmission electron microscopy (TEM).

The working electrodes were made from a mixture of the Fe_3O_4 samples, super-P acetylene black and polyvinylidene fluoride (PVDF). They were blended in solvent of N-methyl-2-pyrrolidinone (NMP) (Aldrich) at a weight ratio of 80:10:10. The slurries of the mixture were coated on a Cu foil and then were dried in a vacuum thermostatic oven at 120°C for 10 h to evaporate the solvent. After that, the foils were tailored into disc shape with a diameter of 10 mm and weighed, which were then used as anode for the LIBs. The precise mass loadings of the active materials in between 1.45-1.65 mg cm^{-2} are designed. Coin cells of 2016-type were used as model and fixed in a glove box protected with Ar. Celgard 2400 membrane has been chosen as separator. 1 mol L^{-1} LiPF$_6$ dissolving in a mixture solvent consisting of ethylene carbonate (EC), dimethyl carbonate (DMC) and ethylene methyl carbonate (EMC) with a volume ratio of 1: 1: 1 was utilized as electrolyte. Metallic lithium layer was utilized as the counter electrode. The charging-discharging processes were tested on a LAND Cell system with a cutoff voltage in between of 3 and 0.01 V. Cyclic voltammetry (CV) measurements were conducted with a CHI760D electrochemical working station by the coin-type cells in configuration of two-electrode with voltages between 0.01 V and 3 V under scan speed of 0.1mV s^{-1}. Electrochemical impedance spectroscopy (EIS) surveys were carried out using the same CHI760D station with frequencies from 100 kHz to 0.01 Hz at an amplitude of 5 mV.

3. RESULTS AND DISCUSSION

3.1. XRD measurements

XRD patterns of $FeC_2O_4 \cdot 2H_2O$ precursor and the as-prepared Fe_3O_4-X have been depicted in Fig. 1. Curve A are the pattern of pure ferrous oxalate dehydrate. In comparison with curve A, both the XRD patterns of Fe_3O_4-12 and Fe_3O_4-36 show the characteristic peaks of $FeC_2O_4 \cdot 2H_2O$ even after 36h

solvothermal treatment. This might be due to the low solubility of ferrous oxalate dihydrate in tetrahydrofuran, which retards the decomposition of $FeC_2O_4 \cdot 2H_2O$ even under such a high temperature and pressure. Partial of the $FeC_2O_4 \cdot 2H_2O$ on the surface of particles have reaction with tetrahydrofuran and transformed into Fe_3O_4, but the internal ones cannot react within 36h. When the reaction time was extended to 72 h, it can be seen the peaks of $FeC_2O_4 \cdot 2H_2O$ disappeared completely (curve D in Figure 1). Differently, the patterns for samples Fe_3O_4-12-500, and Fe_3O_4-36-500 show only the characteristic peaks at $2\theta = 30.01°$, $35.42°$, $43.05°$, $56.94°$ and $62.51°$, and they can be indexed to the (220), (311), (400), (511) and (440) planes of Fe_3O_4 crystal (JCPDS, No. 19-0629). Obviously, no peeks of $FeC_2O_4 \cdot 2H_2O$ can be observed in the curves of E and F. The change of the XRD patterns suggest that the $FeC_2O_4 \cdot 2H_2O$ residues have pyrolyzed during the calcination process at 500 °C [6,7].
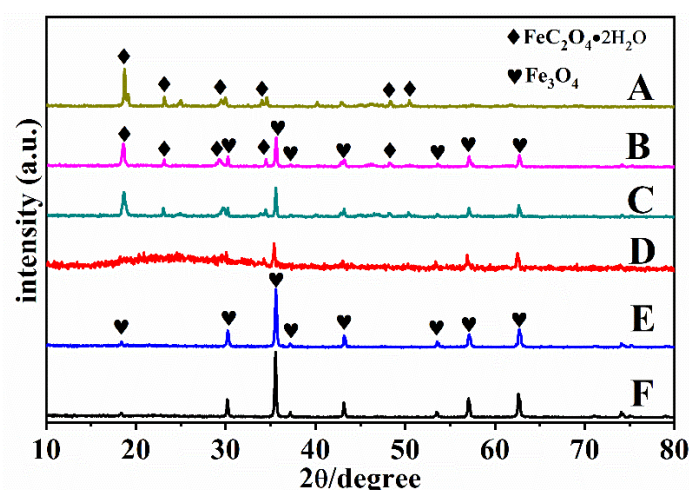
Figure 1. XRD patterns of (A) $FeC_2O_4 \cdot 2H_2O$, (B) Fe_3O_4-12, (C) Fe_3O_4-36, (D) Fe_3O_4-72, (E) Fe_3O_4-12-500, (F) Fe_3O_4-36-500.

3.2. SEM and TEM investigations

Figure 2 show the SEM micrographs of $FeC_2O_4 \cdot 2H_2O$ precursor and the Fe_3O_4 derived with different solvothermal treatment time and temperatures. Fig. 2(A) depicts the picture of ferrous oxalate dehydrate reagent, which reveals large particles with irregular morphology. Figure 2(B) presents the SEM images of the sample obtained via a solvothermal treatment at 300°C for 12h. A few rods structure formed under such a condition, however, it shows irregular and fluffy morphology as the $FeC_2O_4 \cdot 2H_2O$ precursor. When the hydrothermal temperature rises to 350 °C and treated under this temperature for only 6h more rods structures appear although the uniformity is a little bit low (image C). By contrast, the sample prepared solvothermally at 350°C for 12h shows almost uniform rod morphology with a uniform length of approximately 2-3μm (image D). After the calcination at 500 °C for 2h, no significant change in morphology has been observed and the nanorod structure can be maintained perfectly after the such a process (image E). In comparison with the Fe_3O_4 nanoparticles, this rod-like structure can provide more voids against the volume changes of Fe_3O_4 during lithium-ions insertion/extraction

process, thus improving the stability of the electrode structure. On the other hand, this structure also can prevent the aggregation, all these might result in superior electrochemical properties [4,9]. Interestingly, with the extension of treating time, nanoplates and octahedral-like structures can be observed in the sample Fe_3O_4-24 (image F). From the image of H it is clear that the Fe_3O_4 octahedrons growing up gradually when the treating time reaches to 36 h. Wonderfully, no obvious morphology change for both Fe_3O_4-24 and Fe_3O_4-36 after calcination (images G and I). At a solvothermal treating time of 72h, all the short rods vanished and only cuboids and octahedrons with larger size can be observed in image J, conforming the morphology evolution upon treating time.
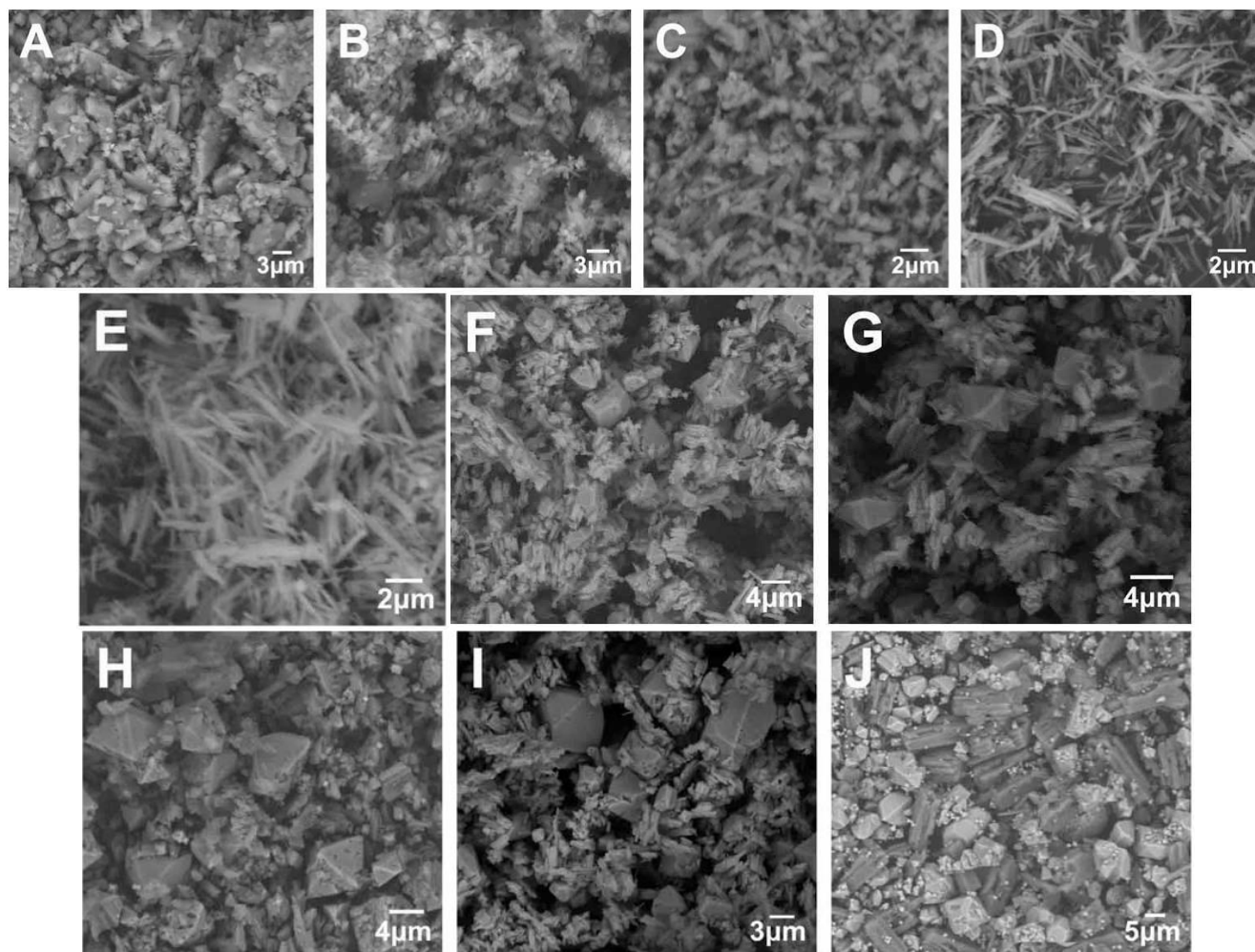

Figure 2. SEM images of (A) $FeC_2O_4 \cdot 2H_2O$, (B) Fe_3O_4-12(300), (C) Fe_3O_4-6, (D) Fe_3O_4-12, (E) Fe_3O_4-12-500, (F) Fe_3O_4-24, (G) Fe_3O_4-24-500, (H) Fe_3O_4-36, (I) Fe_3O_4-36-500, (J) Fe_3O_4-72.

TEM images of Fe_3O_4-12-500 at different magnifications have been depicted in Figure 3. The nanorods with dimeters from few tens to several hundred nanometers and length in between 2-3µm can be observed in the pictures, which is in accordance with the SEM results. From the high resolution picture one can see the nanorods are consisting of Fe_3O_4 nanocrystal with size of about few tens nanometers. There are abundant pores among the nanoparticles. This structure allows easier and faster
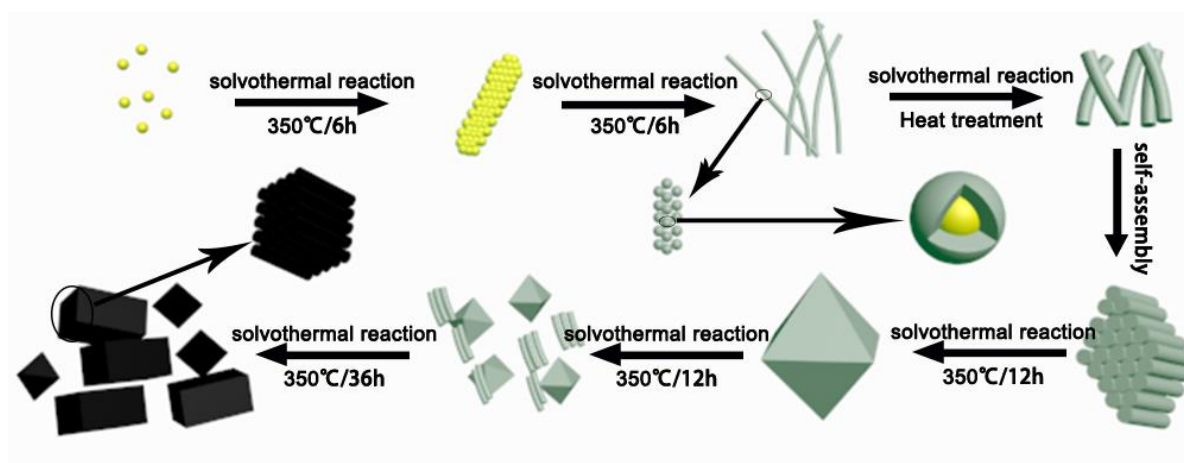
Int. J. Electrochem. Sci., 16 **(2021)** Article ID: 210743

6

penetration of the electrolyte, improves the redox activity of the Fe_3O_4 nanoparticles, relieves the stress generated by volume expansion during lithiation, and promotes the transport of Li^+ [7,12].
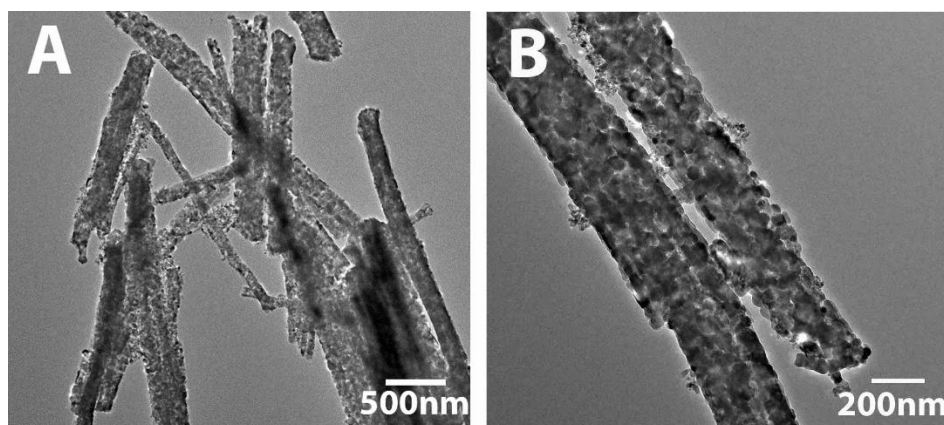
Figure 3. TEM images of Fe_3O_4-12-500 sample under different magnifications.

3.3. The evolution of morphologies

**Figure 4.** Schematic drawing for the formation mechanism of Fe_3O_4-12 nanorods and Fe_3O_4-72 polyhedrons.

The formation process of Fe_3O_4 nanorods and Fe_3O_4 polyhedrons can be speculated as following (Figure 4). First the $FeC_2O_4 \cdot 2H_2O$ crystals dispersed into tetrahydrofuran and formed a suspension, meanwhile the $FeC_2O_4 \cdot 2H_2O$ regrow at elevated temperature of 350 °C and under the autogenic high pressure therein. Then the irregular particles turn to irregular and fluffy rods approximately in the first few hours in the tetrahydrofuran solvent. Such a transition can be supported by the color change of the suspension from light yellow to brownish. Gradually, most of the particles $FeC_2O_4 \cdot 2H_2O$ turn into nanorods in the following six hours. At the same time, the color of the suspension transforms from brownish to grey. After a calcination at 500 °C in N_2 atmosphere, the residual of $FeC_2O_4 \cdot 2H_2O$ decomposed and then the Fe_3O_4-12-500 nanorods were obtained. With the increase of the solvothermally treating time, the nanorods stick together and form plate structures. With the regrowth going on, more

rods aggregated together and the plates began to transform into the octahedrons through the self-assembly and Ostwald ripening effects in the next 24h. Step by step, all the sticks converted into cuboids in the following 36h. Finally, the Fe_3O_4 polyhedrons consist of cuboids and octahedrons were synthesized.

3.4. Porosity characters
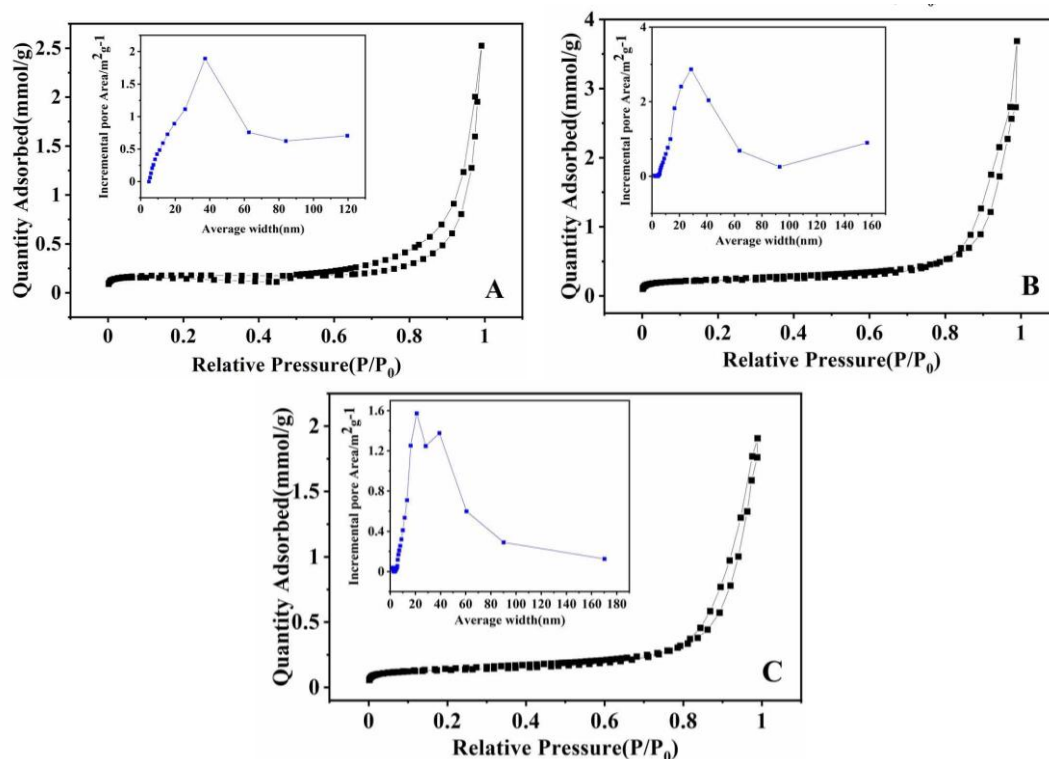
Figure 5. Isotherms of N_2 sorption and curves of pore size distribution (the inset) of (A) Fe_3O_4-12, (B) Fe_3O_4-12-500, (C) Fe_3O_4-72.

N_2 adsorption-desorption measurements have been carried out to learn the specific surface area and pore size distribution of the Fe_3O_4-X samples derived from different time of solvothermal treatment. The measurements have been displayed in Figure 5. It reveals that the Fe_3O_4-12 sample possesses a BET specific surface area of 13.1 m^2 g^{-1}, which is a little bit lower than the value of 18.7 m^2 g^{-1} for Fe_3O_4-12-500. The slight increase of the specific surface area of Fe_3O_4-12-500 can be attributed to the decomposition of ferrous oxalate dihydrate residual and the removal of some organic impurities during the high temperature calcination. The dominant pore size of Fe_3O_4-12-500 was 28.5 nm which smaller than that of 37 nm for Fe_3O_4-12. The shrinking of pores can be due to the condensation taking place during calcination. The Fe_3O_4-72 shows a specific surface area of 11 m^2 g^{-1} and an average pore size distribution of 30 nm. From the comparison one can see that Fe_3O_4-12 sample possess a higher specific area than that of Fe_3O_4-72. The decrease of specific surface area with the increasing of solvothermally treating time can be ascribed to the complete consumption of $FeC_2O_4 \cdot 2H_2O$ and the recrystallization the Fe_3O_4 particles, which is agree with the XRD and SEM investigation. The smaller specific surface area

of Fe3O4-X samples is due to the larger average particle size. We know from the relevant literature that larger pore size is more beneficial to alleviate the volume expansion during lithium embedding of Fe_3O_4, maintain the stability of the electrode structure and improve the electrochemical performance [2,18].

3.5. Electrochemical properties
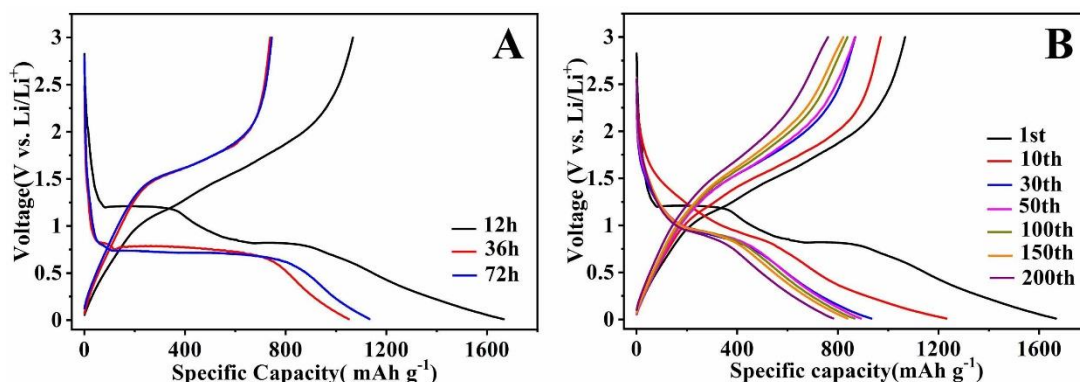
Figure 6. (A) Profiles of the initial discharge-charge process for Fe_3O_4-12-500, Fe_3O_4-36-500 and Fe_3O_4-72 at current density of 200 mA g^{-1}, (B) The discharge/charge profiles of Fe_3O_4-12-500 at different cycles under current density of 200 mA g^{-1}.

The initial charge-discharge voltage profiles of the samples Fe_3O_4-12-500, Fe_3O_4-36-500 and Fe_3O_4-72 were measured under current density of 200 mA g^{-1}. As been depicted in Figure 6A, all the charge-discharge curves show a cliffy voltage fall in between 2.5 and 0.85 V, which is ascribed to the insertion of Li^+ into Fe_3O_4, i.e. $Fe_3O_4 + xLi^+ + xe^- \leftrightarrow Li_xFe_3O_4$ [18, 19]. The voltage at about 1.2V for the sample Fe_3O_4-12-500 might be caused by the interaction between electrolyte and the Fe_3O_4 consisting of the rods. The smooth discharging plateau at potential about 0.85 V can be ascribed to the reduction of iron ions and the formation of nanosized Fe metal and amorphous Li_2O via the redox reaction[20-23]. The initial capacities of Fe_3O_4-12-500 were calculated to be 1666 mAh g^{-1} for the discharge process and 1070 mAh g^{-1} for the charge step, which are superior than those of Fe_3O_4-36-500 (1094 and 731 mAh g^{-1}) and Fe_3O_4-72 (1132 and 748 mAh g^{-1}) at the same current density. Figure 6B shows the discharge/charge profiles of Fe_3O_4-12-500 nanorods at different cycles under density of 200 mA g^{-1}. A high capacity of 791mAh g^{-1} could be delivered under 200 mA g^{-1} after 200 discharge/charge cycles. It demonstrates that the Fe_3O_4-12-500 with a rod nanostructure could enhance the electrochemical performances of Fe_3O_4.

The reversible capacities versus cycling numbers of Fe_3O_4-12-500, Fe_3O_4-36-500 and Fe_3O_4-72-500 have been depicted in Figure 7A. The reversible capacity of Fe_3O_4-12-500 is of 807.9 mAh g^{-1} even after 200 cycles, and the coulombic efficiencies still remained more than 98%. However, the reversible capacity faded quickly to 402 mAh g^{-1} for Fe_3O_4-12-500 and 300.8 mAh g^{-1} for Fe_3O_4-500 after 200 cycles under the same current density. The distinction of the cycle stability among them should contribute to the structure differences of the rods and the polyhedrons. Firstly, the rod structure shows the larger surface area which will be conductive to the insertion/extraction processes of Li ion. Secondly,

the nanorods can smooth the volume changes of the Fe_3O_4 nanocrystal during the Li^+ insertion-desertion process by adjusting its size. Thirdly, it also can relieve the agglomeration of Fe_3O_4 nanoparticles owe to the rod shaped structure [24-26]. The Fe_3O_4 polyhedrons show a low capacity might be due to the closely packing of the Fe_3O_4 nanocrystals in them which induce a low surface area [27, 28]. The rate ability of the Fe_3O_4 with a rod structure is revealed in Figure 7B. The capacities of 970 mAh g^{-1} under 0.1 A g^{-1}, 900 mAhg^{-1} under 0.2 A g^{-1}, 790 mAh g^{-1} under 0.5 A g^{-1}, 600 mAh g^{-1} under 1 A g^{-1} and 360 mAh g^{-1} under 2 A g^{-1} are presented by the Fe_3O_4-12-500 sample. The capacity could go back to the original values as the current rates are restored, showing high reversibility of the Fe_3O_4-12-500 electrode and the potential application to high performance LIBs as anode materials.
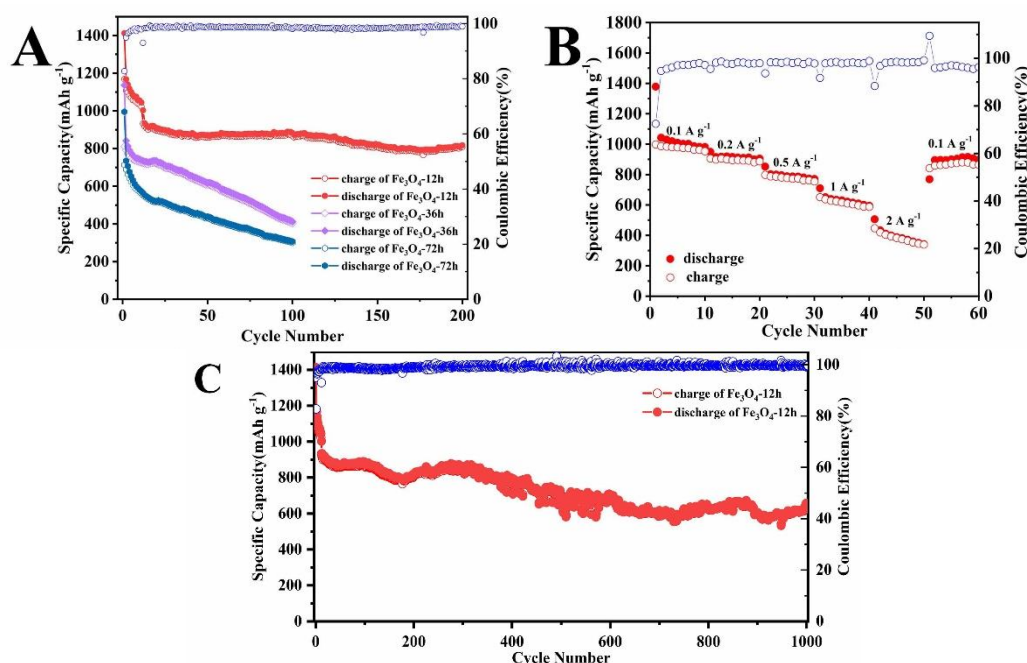

Figure 7. (A) Performances of cycling for Fe_3O_4-12-500, Fe_3O_4-36-500 and Fe_3O_4-72 under current density of 200 mA g^{-1}, (B) The rate performance of Fe_3O_4-12-500. (C) Cycling performance and Coulombic efficiency of Fe_3O_4-12-500.

Figure 7C reveals the performance of long cycle for the Fe_3O_4-12-500 nanorods. After 1000 rounds, the Fe_3O_4 nanorods still can deliver a discharge capacity of 645.5 mAh g^{-1} and a charging capacity of 641.3 mAh g^{-1} with an average coulombic efficiency near 99%, which can be owe to the rod structure of Fe_3O_4-12-500, the in-situ modification with carbon and the good interfacial stability with the electrolyte.

To illustrate further the differences of these Fe_3O_4 samples prepared at different solvothermal treating times, electrochemical impedance spectroscopy (EIS) tests are conducted to the electrodes made of Fe_3O_4 with different morphologies in a frequency between 10^5 and 0.01 Hz. The tests were conducted before the test of galvanostatic cycles and typical EIS plots derived from Fe_3O_4-12-500, Fe_3O_4-36-500 and Fe_3O_4-72 are shown in Figure 8. The EIS has also been simulated using the Z-view software based

on the equivalent circuit (please refer to the inset in Figure 8). As for the equivalent circuit, R_Ω is the overall ohmic resistance, including the resistances from the electrolyte, separator, and electrical contacts, while R_{ct} represents the resistance of charge transfer. CPE is a constant phase element which means the capacitance of double layer. W stands for the Warburg impedance, which presents the diffusion of Li^+ into the bulk active materials under the solid state. The EIS plots for all these three samples display similar shapes. They all show a semicircle in the region of high-middle frequency, which can be attributed to the resistance of charge transfer i.e. R_{ct}. Meanwhile, the titled line in the region of low frequency can be assigned to the Warburg impedance [29-31]. From the comparison of the plots of these samples one can see the diameter of the semicircle increases in series of Fe_3O_4-12-500, Fe_3O_4-36-500 and Fe_3O_4-72, demonstrating Fe_3O_4-12-500 possess the lowest charge transfer resistance among them[32-34]. The high conductivity of Fe_3O_4-12-500 can be due to the nanorod structure which forms conducive networks. Another possibility is the modification of carbon. The element analysis tests reveal that the carbon content in Fe_3O_4-12-500 is about 1.0 wt%, which is higher than that 0.8wt% for Fe_3O_4-36-500 and 0.6wt% in Fe_3O_4-72. Obviously. the Fe_3O_4-12-500 contain more carbon that the other twos. All these characters play roles together, which then enhance effectively the electrochemical properties of the Fe_3O_4-12-500 sample.
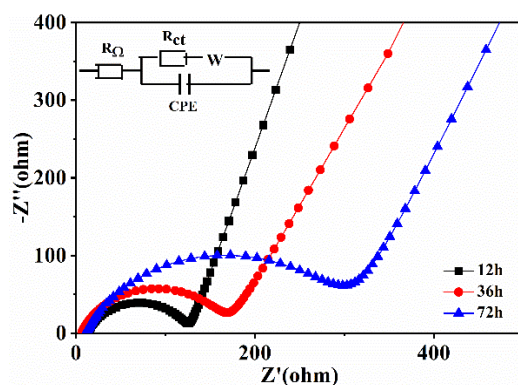
Figure 8. The Nyquist plots of Fe_3O_4-12-500, Fe_3O_4-36-500 and Fe_3O_4-72.

The CV curves of the electrodes made of Fe_3O_4 with different morphologies are presented in Figure 9. The first five cycles in voltage span from 0.01 to 3 V under a scan steep of 0.1 mV s^{-1} have been recorded. The intense peak around 0.53V in the CV curves of the 1st discharge process for Fe_3O_4-12-500 can be ascribed by the formation of solid electrolyte interface (SEI). The peak disappears in the following cycles. The peak observed at 0.58V for the Fe_3O_4-12-500 and at 0.50V for Fe_3O_4-72 can be assigned to the lithiation reaction of $Fe_3O_4+ 8Li^++8e^-\leftrightarrow 3Fe^0+ 4Li_2O$[35, 36]. The observed main anodic peaks at about 1.67V for Fe_3O_4-12-500, at 1.65V for Fe_3O_4-36-500 and around 1.66V for Fe_3O_4-72 can be designated to the oxidation of Fe^0 to Fe^{2+} and Fe^{3+} in the anodic processing. In the following scans, peak potentials for both of the cathodic and anodic ones move to higher voltage because of the polarization of the active materials after the first cycle [37]. The peak intensity is tended to stable after

three cycles, and it can be found that the intensities of peaks for Fe₃O₄-12-500 are the most intense one among these three samples, revealing that this sample possesses superior lithium storage ability.
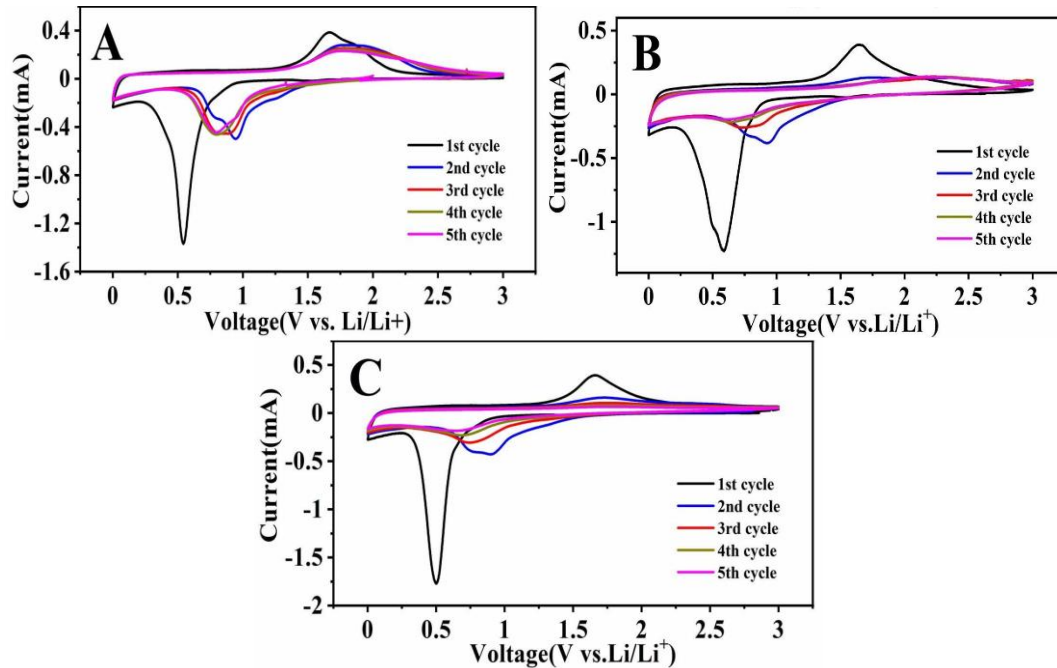
Figure 9. The Cyclic voltammogram (CV) curves for (A) Fe₃O₄-12-500, (B) Fe₃O₄-36-500 and (C) Fe₃O₄-72.

Table 1. Electrochemical preformances of Fe₃O₄-12-500 nanorod anode

Composites	Rate performance		Cycle performance			Ref.
	Capacity (mAh·g⁻¹)	Current density (mA • g⁻¹)	Final capacity (mAh·g⁻¹)	Current density (mA • g⁻¹)	Cycle	
Fe₃O₄ nanospheres	631	2000	743	200	100	[3]
Fe₃O₄@C	431	2 C	642	0.2 C	1000	[4]
Fe₃O₄@C nanofibers	503	1000	762	500	300	[7]
Fe₃O₄/RGO	410	1000	832	100	40	[17]
Fe₃O₄@C nanorods	630	1000	762	100	50	[37]
Fe₃O₄@C	573	1500	573	100	100	[38]
Fe₃O₄@C/CNTs	282	1200	693	300	200	[39]
Fe₃O4@C	317	2000	216	2000	800	[40]
Fe₃O₄ nanowires	557	2000	900	200	100	[41]
Fe₃O₄@C	430	1000	860	200	300	[42]
Fe₃O₄ nanorods	360	2000	650	200	1000	This work

In comparison to some of the documented date, the Fe_3O_4-12-500 nanorods anode of this work exhibits competitive electrochemical performance in terms of specific capacity and cycle life (see Table 1). Therefore, the Fe_3O_4 nanorod composites prepared by the high temperature solvothermal method contains a potential role in further development of anode materials for superior lithium-ion batteries.

4. CONCLUSIONS

Fe_3O_4 with superior electrochemical performance as anode for LIBs are fabricated via a solvothermal method at high temperature up to 350℃ using $FeC_2O_4 \cdot 2H_2O$ as precursor. With the increase of solvothermal treating time from 12h to 72h, the morphologies of the obtained Fe_3O_4 samples changed gradually from nanorods to nanoplates and finally to polyhedrons. The Fe_3O_4-12-500 nanorods shows higher capacity and better cycling ability than those presented by Fe_3O_4-36-500 plates and Fe_3O_4-72 polyhedrons. Control experiments demonstrated that the Fe_3O_4-12-500 nanorods, which is prepared through solvothermal treatment for 12h, possesses the best electrochemical properties. A high capacity of 807.9 mAh g^{-1} has been retained when cycled for 200 rounds under a current density of 200 mA g^{-1} and a satisfied capacity of 641.3 mAh g^{-1} could still be remained even after 1000 cycles. The excellent electrochemical performance of the Fe_3O_4-12-500 sample can be ascribed on the one hand to the rod structure which could play role as conductive network and on the other hand to the in-situ carbon modification achieved by pyrolyzing the organic moieties in the precursor of $FeC_2O_4 \cdot 2H_2O$ which can improve the conductivity as well. We believe that the methodology developed herein could be extended to the preparation of other kinds of oxides of transition metal as anode materials for LIBs.

References

1.   X. Men, T. Wang, B. Xu, Z. Kong, X. Liu, A. Fu, Y. Li, P. Guo, Y. Guo, H. Li, X. S. Zhao, *Electrochim. Acta*, 324 (2019) 134850.
2.   T. Wang, X. Yu, M. Fan, Q. Meng, Y. Xiao, Y. X. Yin, H. Li, Y. G. Guo, *Chem Commun (Camb)*, 56 (2019) 245.
3.   H. Zhang, *Int. J. Electrochem. Sc.* (2020) 4789.
4.   H. Lv, *Int. J. Electrochem. Sc.* (2020) 2157.
5.   Y. Huangfu, C. Liang, Y. Han, H. Qiu, P. Song, L. Wang, J. Kong, J. Gu, *Compos. Sci. Technol.*, 169 (2019) 70.
6.   S. Zhou, Y. Zhou, W. Jiang, H. Guo, Z. Wang, X. Li, *Appl. Surf. Sci.*, 439 (2018) 927.
7.   Q. Wu, R. Zhao, X. Zhang, W. Li, R. Xu, G. Diao, M. Chen, *J. Power Sources*, 359 (2017) 7.
8.   S. Zhou, *Int. J. Electrochem. Sc.* (2021) 210461.
9.   L. Li, H. Wang, Z. Xie, C. An, G. Jiang, Y. Wang, *J. Alloy. Compd.*, 815 (2020) 152337.
10.   L. Wang, L. M. Housel, D. C. Bock, A. Abraham, M. R. Dunkin, A. H. Mccarthy, Q. Wu, A. Kiss, J. Thieme, E. S. Takeuchi, A. C. Marschilok, K. J. Takeuchi, *ACS Appl. Mater. Inter.*, 11 (2019) 19920.
11.   M. Zou, L. Wang, J. Li, L. Guan, Z. Huang, *Electrochim. Acta*, 233 (2017) 85.

12.　　L. Jing, A. Fu, H. Li, J. Liu, P. Guo, Y. Wang, X. S. Zhao, *RSC Adv.*, 4 (2014) 59981.
13.　　Y. Guo, D. Zhang, Y. Yang, Y. Wang, Z. Bai, P. K. Chu, Y. Luo, *Nanoscale*, 13 (2021) 4624.
14.　　H. Wu, N. Du, J. Wang, H. Zhang, D. Yang, *J. Power Sources*, 246 (2014) 198.
15.　　C. Sun, X. Zheng, T. Sun, Z. Xu, Y. Yuan, X. Liu, A. Fu, H. Li, *Int. J. Electrochem. Sc.* (2020) doi: 10.20964/2021.05.53.
16.　　F. Ke, L. Huang, B. Zhang, G. Wei, L. Xue, J. Li, S. Sun, *Electrochim. Acta*, 78 (2012) 585.
17.　　P. Lian, X. Zhu, H. Xiang, Z. Li, W. Yang, H. Wang, *Electrochim. Acta*, 56 (2010) 834.
18.　　P. Wang, M. Gao, H. Pan, J. Zhang, C. Liang, J. Wang, P. Zhou, Y. Liu, *J. Power Sources*, 239 (2013) 466.
19.　　L. Wang, Y. Yu, P. C. Chen, D. W. Zhang, C. H. Chen, *J. Power Sources*, 183 (2008) 717.
20.　　Z. Zeng, H. Zhao, J. Wang, P. Lv, T. Zhang, Q. Xia, *J. Power Sources*, 248 (2014) 15.
21.　　Y. C. Dong, R. G. Ma, M. Jun Hu, H. Cheng, C. K. Tsang, Q. D. Yang, Y. Yang Li, J. A. Zapien, *J. Solid State Chem.*, 201 (2013) 330.
22.　　S. M. Yuan, J. X. Li, L. T. Yang, L. W. Su, L. Liu, Z. Zhou, *ACS Appl. Mater. Inter.*, 3 (2011) 705.
23.　　T. Zhang, C. Yang, S. Sun, Y. Huang, G. Meng, A. Han, J. Liu, *Science China Materials* (2020).
24.　　Z. Hu, H. Cui, J. Li, G. Lei, Z. Li, *Ceram. Int.*, 46 (2020) 18868.
25.　　D. Su, H. Ahn, G. Wang, *J. Power Sources*, 244 (2013) 742.
26.　　X. Yao, C. Tang, G. Yuan, P. Cui, X. Xu, Z. Liu, *Electrochem. Commun.*, 13 (2011) 1439.
27.　　S. Jia, T. Song, B. Zhao, Q. Zhai, Y. Gao, *J. Alloy. Compd.*, 585 (2014) 580.
28.　　L. Zhao, H. Zhang, J. Tang, S. Song, F. Cao, *Mater. Lett.*, 63 (2009) 307.
29.　　B. Wang, G. Wang, Z. Zheng, H. Wang, J. Bai, J. Bai, *Electrochim. Acta*, 106 (2013) 235.
30.　　D. Zhang, Y. J. Mai, J. Y. Xiang, X. H. Xia, Y. Q. Qiao, J. P. Tu, *J. Power Sources*, 217 (2012) 229.
31.　　M. Yan, G. Li, J. Zhang, Y. Tian, Y. Yin, C. Zhang, K. Jiang, Q. Xu, H. Li, Y. Guo, *ACS Appl. Mater. Inter.*, 12 (2020) 27202.
32.　　C. Wang, H. Li, A. Fu, J. Liu, W. Ye, P. Guo, G. Pang, X. S. Zhao, *New J. Chem.*, 38 (2014) 616.
33.　　S. Wang, J. Zhang, C. Chen, *J. Power Sources*, 195 (2010) 5379.
34.　　X. Men, X. Kong, X. Yang, B. Wang, Y. Wang, Y. Liu, L. Yu, H. Li, B. Xu, *Int. J. Hydrogen Energ.* (2020).
35.　　Y. Guo, D. Zhang, Y. Yang, Y. Wang, Z. Bai, P. K. Chu, Y. Luo, *Nanoscale*, 13 (2021) 4624.
36.　　H. Li, J. Wang, Y. Li, Y. Zhao, Y. Tian, I. Kurmanbayeva, Z. Bakenov, *J. Electroanal. Chem.*, 847 (2019) 113240.
37.　　Q. Q. Xiong, Y. Lu, X. L. Wang, C. D. Gu, Y. Q. Qiao, J. P. Tu, *J. Alloy. Compd.*, 536 (2012) 219.
38.　　Y. Zhang, Y. Li, H. Li, Y. Zhao, F. Yin, Z. Bakenov, *Electrochim. Acta*, 216 (2016) 475.
39.　　J. Liu, J. Ni, Y. Zhao, H. Wang, L. Gao, *J. Mater. Chem. A*, 1 (2013) 12879.
40.　　M. Liu, H. Jin, E. Uchaker, Z. Xie, Y. Wang, G. Cao, S. Hou, J. Li, *Nanotechnology*, 28 (2017) 155603.
41.　　Y. Wang, Y. Jin, M. Jia, *Mater. Lett.*, 228 (2018) 395.
42.　　J. Xu, J. Zhang, C. Wang, *Int. J. Appl. Ceram. Tec.*, 14 (2017) 938.